Electron identification and multi-dimensional unfolding studies on ALICE

Christian Nesenberend
Universiteit Utrecht
Supervisor:
Hongyan Yang

June 25, 2014

Abstract

In this thesis, a study of electron measurement in Pb-Pb collisions at 2.76 TeV with the ALICE experiment is presented. First electron identification methods are studied with two sets of cuts, making use of the Time Projection Chamber (TPC), Time-of-Flight (TOF) and Inner Tracking System (ITS) detectors. Methods of unfolding of the p_T, η, ϕ spectrum of electrons are discussed, including a 3-dimensional Bayesian unfolding method and a minimization unfolding method. These methods are applied to simulated data and compared with the MC spectrum. The Bayesian method is applied to real data afterwards.

Contents

Chapter 1

Motivation

Mankind has always been curious about how the universe started. Many religions are claiming that it started with the touch of a creator, which created everything we know. Others have been arguing that the universe has always existed, and will always exist. This debate has been going on for centuries.

However, the arguments were almost all philosophical, until Albert Einstein created his theory of general relativity. From his theory Alexander Friedmann derived that the universe should be an expanding system. Edwin Hubble supported this idea with observation of effects of an expanding universe. His observations are some of the first physical evidence found against a static universe.

A later breakthrough was the observation of the cosmic microwave background. This background shows us that the very early universe was dense and hot. Such extreme energies are rarely found now, except in relativistic heavy ion collisions, such as those prodcued at the LHC at CERN.

At CERN, ions are accelerated to relativistic speeds. These collisions cause extreme physical conditions, similar to those just after the Big Bang [11]. At such extreme energies quarks are freed from their bonds in hadrons (p,n, etc). This 'soup' of free quarks is called a Quark-Gluon Plasma (QGP).

One of the subdetectors of the LHC, A Large Ion Collider Experiment (ALICE), is designed to study the states of matter in relativistic ion collisions, such as QGP[12]. A commonly used way to look at these kind of material states, QGP in particular, is to look at the photons emitted in the collision. Photons do not interact strongly, so they will not interact with the matter in different phases as they pass through it(see figure 1.1 for the aftermath of a collsion).

To measure photons different methods are used, but a regularly used method is by looking at virtual photon conversions:

$$\gamma^* \rightarrow e^+ + e^-$$

By looking at correlated dielectron pairs with very small invariant mass we have access to the production of photons. This means that the measurement of electrons and positrons is a first step for measuring the photons, which is a step in measuring the properties of the QGP.

In this thesis, a study of electron measurement in Pb-Pb collisions at 2.76 TeV with the ALICE experiment is presented. First electron identification methods are studied with two sets of cuts, making use of the Time Projection Chamber (TPC), Time-of-Flight (TOF) and Inner Tracking System (ITS) detectors.
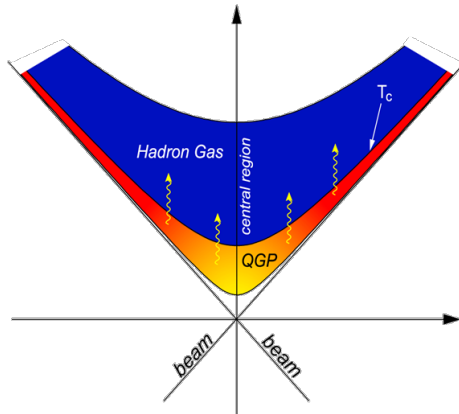
Figure 1.1: The evolution of a QGP created after a collision.[13]

Methods of unfolding of the p_T, η, ϕ spectrum of electrons are discussed, including a 3-dimensional Bayesian unfolding method and a minimization unfolding method. These methods are applied to simulated data and compared with the MC spectrum. The Bayesian method is applied to real data afterwards.

Chapter 2

Data Analysis

2.1 The ALICE Experiment

ALICE is one of the detectors at the Large Hadron Collider (LHC)[14]. It is focused on heavy-ion collisions, and has many detectors, including a central barrel, which consists of the detectors ITS, TPC, TOF, HMPID, EMCAL, PHOS and muon detectors, and a forward muon spectrometer, as shown in figure 2.1. The studies performed in this thesis are done within the central barrel of ALICE. In this thesis, the detectors Inner Tracking System(ITS),a Time Projection Chamber(TPC) and Time of Flight(TOF) are used for elctron identification. These detectors are explained more detail in this section.

2.1.1 TPC

The Time Projection Chamber (TPC) consists of a chamber filled with 90% neon and 10% CO2, with readout chambers at the ends and in the middle, with an electric field. [2]

When a particle enters the TPC, it will ionizes the gas present. The electric field causes the electrons to move towards the readout chambers. At the readout chambers, an avalanche is caused, which will create a peak in the electric signal of the anode. The location of the signal indicates the ϕ and the r coordinates of the tracklet, but not the coordinate along the beam axis.

By measuring the time it takes for the ionized gas to drift towards the readout chambers, we can get the z coordinate. Integrating the drift velocity over time results in the location of the ionization. Since all coordinates are known, the path of the particle can be tracked through TPC. Using the curvature of the track (thanks to the magnetic field), the momentum can be determined. [1]

The TPC still gives more information, namely the height of the peak of the anode. This height is proportional to the energy loss of the track, $\frac{dE}{dx}$. The energy loss of high-energy particles in materials has been heavily studied. For instance, the Bethe-Bloch formula describes the energy loss for bigger particles[1]:

$$\frac{dE}{dx} = \frac{4\pi}{m_e c^2} \cdot \frac{nz^2}{\beta^2} \cdot \left(\frac{e^2}{4\pi\varepsilon_0} \right)^2 \cdot \left[\ln\left(\frac{2m_e c^2 \beta^2}{I \cdot (1 - \beta^2)} \right) - \beta^2 \right]$$
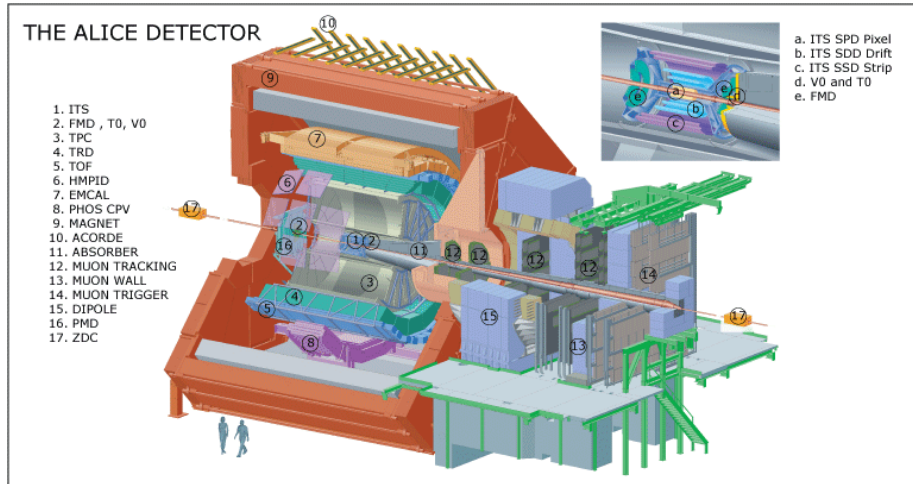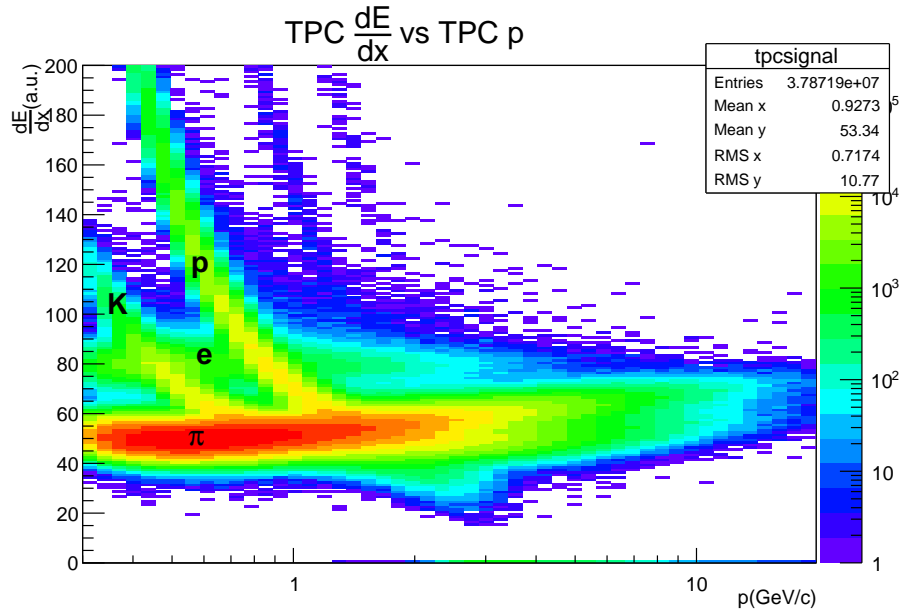
Figure 2.1: An overview of ALICE

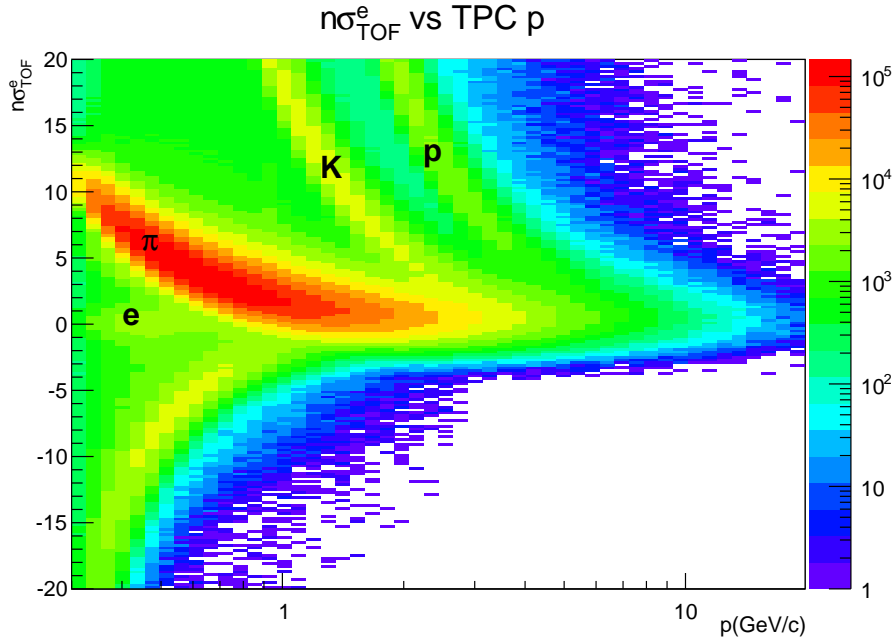Figure 2.2: The $\frac{dE}{dx}$ measurement of TPC plotted versus TPC momentum.

Figure 2.3: $n\sigma^{e}_{\mathrm{TOF}}$ versus TPC momentum.

with n the electron density and z the charge of the particle moving through the gas. For electrons at lower momenta corrections to the Bethe-Bloch are needed as they are smaller particles so they interact differently with matter. Figure 2.2 illustrates that the different energy loss of different particles can also be seen in TPC. The TPC signal of different particles can be distinguished, but there are regions in which some of the particle distributions overlap.

So it is possible to predict the energy loss for particles with known momentum, mass and charge. We can compare this with the measured result using the relative deviation of the measured enegy loss from the expected one, normalized by the detector resolution, defined as: [3]:

$$n\sigma^{\mathrm{x}}_{\mathrm{TPC}} = \frac{\left(\frac{dE}{dx}\right)_{\mathrm{TPC\ measured}} - \left(\frac{dE}{dx}\right)_{\mathrm{expected\ for\ x}}\left(p_{\mathrm{TPC\ measured}}\right)}{\sigma}$$

with σ the detector resolution of TPC. The mean of the distribution of $n\sigma^{\mathrm{x}}_{\mathrm{TPC}}$ for particle x is not exactly 0, as the calbiration of the TPC $\frac{dE}{dx}$ models is not perfect.

2.1.2 TOF

The Time-Of-Flight (TOF) detector (as shown in figure 2.1) measures the time when a particle passes through it. This measurement is also done by looking at the ionization trail caused by the particle. The electrons freed by the particle directly cause a shower, which is stopped by a resistive plate (as shown in figure 2.4). This happens multiple times during the passing of the particle, so an electrical signal is measured when the particle passes.[4]
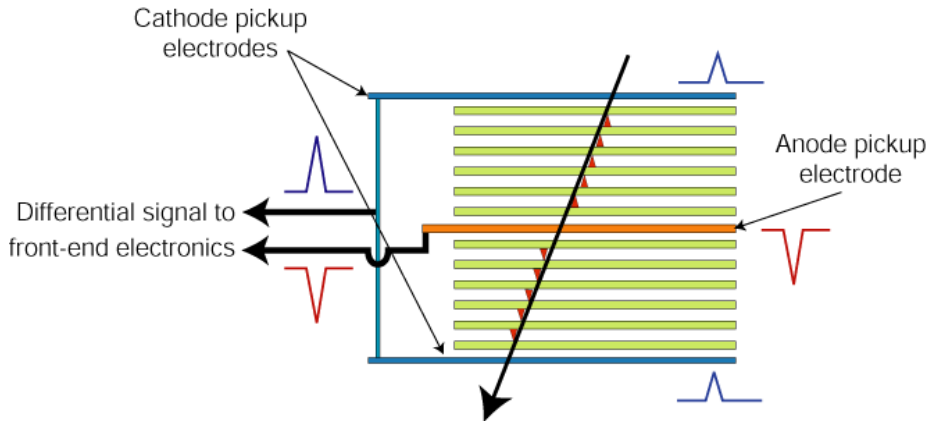
Figure 2.4: An illustration of the principle on which TOF depends[4]

Using the momentum and a suspected mass we can predict the time the track takes to move from the collision to the TOF, ΔT. If we use the measured time of collision T_{collsion}, the same information can be measured. We can define a similar $n\sigma$ for TOF[3]:

$$n\sigma^{\text{x}}_{\text{TOF}} = \frac{(T_{\text{TOF measured}} - T_{\text{collision}}) - \Delta T_{\text{expected for x}}(p_{\text{measured}}, l)}{\sigma}$$

with l the track length and σ the combined detector resolution. This combined detector resolution is the detector resolution of TPC $T_{\text{collision}}$ and the influence of l on ΔT. This enables us to seperate other particles from electrons, as shown in figure 2.3, where individual particles can be distinguished. This figure also shows that TOF can be used to seperate electrons from kaons and protons.

2.1.3   ITS

The Inner Tracking System (ITS) is the detector closest to the beam in ALICE. It is used to assist the TPC in tracking and for particle identification. It consists of 6 layers of silicon detectors, with each 2 layers a different detector type. This can be seen in the smaller figure in figure 2.1.

The two innermost layers to the beam are the Silicon Pixel Detectors (SPD). Like the other detectors used in my thesis they work by measuring the electron showers generated by the ionization of silicon by particles. The amount of pixels(256 circular $\times$ 32 rows) enables precise tracking close to the beam.[5] They are used for tracking, and requiring a hit in the first SPD layer helps remove secondary particles created in ALICE.

The second two layers are the Silicon Drift Detectors (SDD). Silicon Drift Detectors are similar to the TPC because they measure the particles by ionization at the end of the chambers, and use the drift time to extract one of the coordinates. They can also measure the energy loss. [1]

The outer two layes are Silicon Strip Detectors (SSD). SSD is very similar to SDD. The difference between them is that charges move towards strips in SSD, instead of the end of the chambers in SDD. [6]
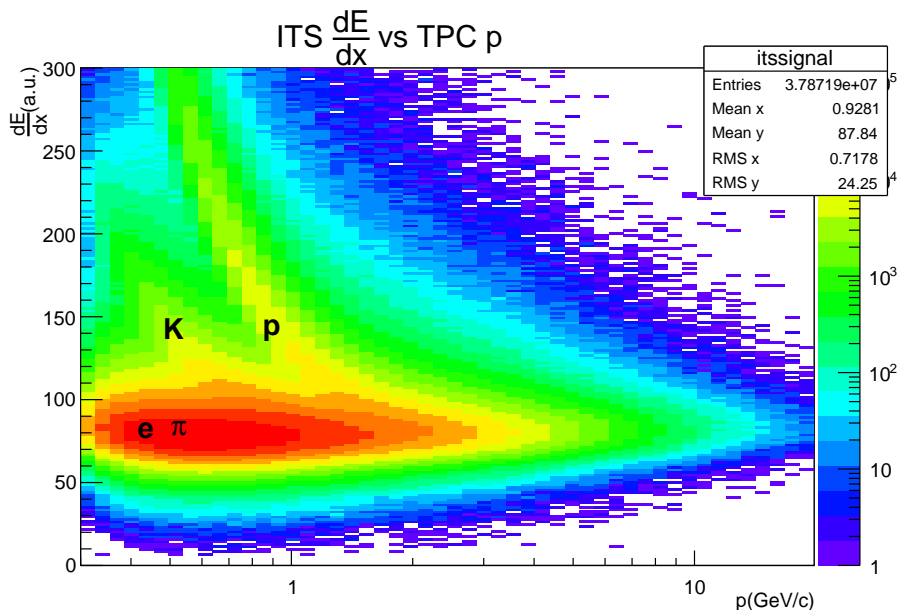
7

Figure 2.5: The $\frac{dE}{dx}$ measurement of ITS versus the TPC momentum.

The energy loss of ITS is shown in figure 2.5. In this figure different particles can be distinguished, although electrons and pions cannot. K and p can still be distinguished at lower momentum.

Similar to the TPC, we can compare the measured $\frac{dE}{dx}$ to the expected $\frac{dE}{dx}$ defining the value[3]:

$$n\sigma_{\text{ITS}}^{\text{x}} = \frac{\left(\frac{dE}{dx}\right)_{\text{ITS measured}} - \left(\frac{dE}{dx}\right)_{\text{Expected for x}}(p_{\text{measured}})}{\sigma}$$

with σ the resolution of ITS.

2.2 Data sample

The analysis jas been performed on two different types of datasets. Monte-Carlo(MC) HIJING Pb-Pb events at 2.7 TeV were used to get the detector response for unfolding (section 2.4), as well as forthe electron particle identification study. The electron PID cut was checked on tested data and then used for unfolding measured electrons produced in real Pb-Pb collisions at TeV, data taken in 2011

2.2.1 Kinematics

For hadron collider experiments, different kinematical properties are used rather then the usual p_x, p_y, p_z. The kinematics that are used more often are p_T, η and ϕ. The transverse momentum p_T is defined as

$$p_T = \sqrt{p_x^2 + p_y^2}$$

The kinematical property ϕ is defined as the angle with the x-axis, which is aligned towards the center of the LHC ring. The pseudorapidity η is not a coordinate seen much outside of particle physics. It is defined as

$$\eta = -\log\left(\tan\left(\frac{\theta}{2}\right)\right)$$

with θ the angle of the momentum with the z-axis, the beam direction. This coordinate is used in particle physics because the particle distribution as a function of η is fairly constant(as can be seen in figure 2.36), and also because it is approximately the Lorentz boost for the coordinate system that makes the particles move only perpendicular to the beam[15].

2.2.2 Event and track quality cuts

Event cuts

We reject events that do not satisfy:

$$N_{\text{contributors to vertex}} > 0$$
$$|z_{\text{vertex}}| < 10cm$$
$$\text{centrality(V0M)} < 10\%$$

The meaning and reasoning behind these requirements are discussed in this section. Only those events where there are tracks which are used determine the vertex($N_{\text{contributors to vertex}} > 0$) are selected. The vertex is the location of the collision. Events are also cut on z_{vertex} to ensure that the event happened within the center of ALICE, so events must have the property that $|z_{\text{vertex}}| < 10cm$.

Centrality is another criteria on which we select our events. Centrality can be best explained as a measure for how offset the two lead ions are if they collide[7]. A centrality of 0 means head-on collision. The centrality can be estimated from the multiplicity distributions of multiple detectors in ALICE. Only central collisions will be considered, so events will be required to have centrality < 10%(using centrality estimator "V0M" to calculate centrality).

2.2.3 Track cuts

For both MC and real data we reject tracks that do not satisfy

$$|\eta| < 0.8$$
$$p_T > 0.3 GeV/c$$
$$\text{track refit in TPC and ITS}$$
$$\chi^2_{\text{ITS}}/N_{\text{Clusters ITS}} < 36$$
$$\chi^2_{\text{TPC}}/N_{\text{Clusters TPC}} < 4$$
$$\text{Hit in the first layer of ITS}$$
$$N_{\text{ITS clusters}} \geq 4$$
$$N_{\text{TPC clusters}} > 70$$
$$N_{\text{crossed rows TPC}}/N_{\text{findable clusters TPC}} > 0.8$$
$$N_{\text{crossed rows TPC}} > 100$$
$$DCA_{xy} < 1cm$$
$$DCA_z < 3cm$$
$$\text{reject kink daughters}$$

The meaning and reasoning behind these requirements are discussed in this section.

The tracks which do not have enough transverse momentum to be detected by TOF are rejected, so only tracks with $p_T > 0.3 GeV/c$ are accepted. To avoid edge effects, only tracks that are well within the acceptance of ALICE detectors in the central barrel are selected. This means tracks with $|\eta| > 0.8$ are rejected.

The tracks are found by fitting in TPC and ITS inward, after which a fit is done outward. Then, the refit is done, which is a fit inward again. Tracks are required to be refit in TPC and ITS. A selection on the fit quality is done by requiring $\chi^2_{\text{ITS}}/N_{\text{Clusters ITS}} < 36$ and $\chi^2_{\text{TPC}}/N_{\text{Clusters TPC}} < 4$ (this χ^2 is the goodness-of-fit χ^2 for the tracks). To reject electrons coming from secondary decays, the tracks are required to have a hit in the first layer of ITS(SPD).

To improve TPC and ITS PID performance, $N_{\text{clusters ITS}} \geq 4$ and $N_{\text{clusters TPC}} > 70$ are required. Further more, tracks are required to satisfy $N_{\text{crossed rows TPC}}/N_{\text{findable clusters TPC}} > 0.8$ and $N_{\text{crossed rows TPC}} > 100$ to improve the TPC momentum resolution. The tracks are required to originate close to the vertex, so $DCA_{xy} < 1cm$ and $DCA_z < 3cm$ are required, where DCA means distance of closest approach to the vertex of the event. The so-called kink daughters are rejected. Kink daughters are particles which are decay products of particles being tracked. For instance, in the TPC a π^+ is tracked, which decays into $e^+\nu_e$ within TPC. Then if this e^+ is tracked, it is a kink daughter[6].

2.3 Electron identification

Using the AliRoot framework, for each detector and a certain particle the number of standard deviations can be retrieved, called $n\sigma^y_X$ for detector X detecting particle y (as described in section 2.1)[3]. These variables are retrieved for electron identification. In MC simulations to amount of electrons in a certain $n\sigma$ region, and the amount of hadrons, can be retrieved. Hadron con-

tamination and PID efficiency are often used to justify the goodness of a PID scheme. Hadron contamination is fraction of tracks which are non-electron, i.e. $N_{\text{non-electron tracks within PID cut}}/N_{\text{tracks within PID cut}}$. PID efficiency is the number of electrons within the PID cut divided by the number of total electrons: $N_{\text{electron tracks within PID cut}}/N_{\text{electron tracks}}$.

For dielectron analysis, it is required that the hadron contamination is no bigger than 10%. In order to achieve this goal, PID schemes has been checked with MC, and corresponding hadron contamination and PID efficiency are compared.

At first, a spherical cut has been considered:

$$(n\sigma^e_{\text{TPC}})^2 + (n\sigma^e_{\text{TOF}})^2 + (n\sigma^e_{\text{ITS}})^2 < 16$$
$$(n\sigma^K_{\text{TPC}})^2 + (n\sigma^K_{\text{TOF}})^2 + (n\sigma^K_{\text{ITS}})^2 > 16$$
$$(n\sigma^p_{\text{TPC}})^2 + (\min(n\sigma^p_{\text{TOF}}, 20))^2/32 + (n\sigma^p_{\text{ITS}})^2 > 16$$
$$n\sigma^e_{\text{TPC}} > -2.7e^{-0.4357p_{\text{TPC}}} \qquad n\sigma^\pi_{\text{TPC}} > 4$$

This set of cuts consists of a spherical inclusion electron cut and spherical rejection cuts for π and K. The minimum in the spherical K rejection is due to a limitation of my analysis task, the saved bin range(this minimum does improve the PID cut quality). Further more, two pion rejection cuts are used. A parametrization of the π rejection cut for real data has been used to reject π. A secondary rejection cut has been used to improve perfomance of the PID in MC analysis.

Another PID method with a less complex parametrization for p(and K) rejection has been checked. This rectangular cut includes:

$$|n\sigma^e_{\text{TPC}}| < 4$$
$$|n\sigma^e_{\text{TOF}}| < 4$$
$$n\sigma^e_{\text{ITS}} < 2.5$$
$$n\sigma^e_{\text{TPC}} > -2.7e^{-0.4357p_{\text{TPC}}} \qquad n\sigma^\pi_{\text{TPC}} > 4$$

This set of cuts consists of a TPC electron inclusion cut, a TOF electron inclusion cut, an ITS electron inclusion cut and the same two pion rejection cuts. The asymmetry in ITS is used to increase PID efficiency, because in the bins in which ITS is useful to reject π and K, the distribution of π and K lies above $n\sigma^e_{ITS} = 0$.

Due to the imperfect PID calibration, the electron distributions of $n\sigma^e_{\text{TPC}}$ and $n\sigma^e_{\text{TOF}}$ are not centered at 0. Because the same cut is required in MC as in real data, a small compensation has been applied to translate the cut used in MC to a cut on real data, as listed in the following:

$$|n\sigma^e_{\text{TPC}} + .3| < 4$$
$$|n\sigma^e_{\text{TOF}} + .2| < 4$$
$$n\sigma^e_{\text{ITS}} < 2.5$$
$$n\sigma^e_{\text{TPC}} > -2.7e^{-0.4357p_{\text{TPC}}}$$

This cut is used to estimate contamination by doing a double Gaussian fit on TPC, on the data that is cut with the ITS and TOF cuts. However, this
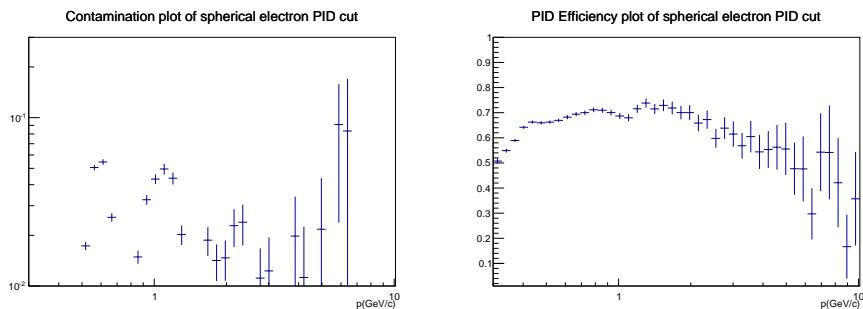
(a) The contamination of the spherical PID cut.
(b) The PID efficiency of the spherical PID cut.

Figure 2.6: The PID efficiency and contamination of the spherical electron PID cut in MC simulations.

contamination estimation does not take into account particles that the TPC can not seperate from electrons, and also does not work when this fit does not convergence correctly.

2.3.1 Results

In figure 2.6a the hadron contamination of the spherical cut is shown, and in figure 2.6b the PID efficiency of this cut. The hadron contamination is always below 10% so the spherical electron PID cut can be used for dielectron analysis. The PID efficiency of the spherical cut is approximately 65% for $p < 2GeV/c$, so the amount of electrons rejected by the spherical PID cut is not very high.

The effect of the spherical cut on the PID response can be seen in figures 2.7, 2.8, 2.9 and 2.10. In figure 2.7 the effects of the TPC pion rejection can be seen, before(left) and after(right) the spherical PID cut. The black line is the imperical parametrization for pion rejection. Protons and kaons are also rejected, which is also illustrated in figure 2.8. This figure further illustrates the effect of the electron inclusion cut, as the kaon, proton and pion distributions are all partly eleminated directly by the cut.

Figure 2.9 further illustrates the reason for use of TOF, as the particles other then the electron have a more widespread distrbution before the spherical PID cut(upper). Figure 2.10 shows that ITS is only useful for certain p bins, as the overall spectrums overlap. However, as shown in figure 2.5, ITS can still be used to reject protons or kaons.

The PID efficiency and hadron contamination of the rectangular electron PID cut are shown in figure 2.11b and 2.11a, respectively. The hadron contamination is slightly worse for the rectangular cut than the spherical cut, but the PID efficiency increases significantly. For the rectangular cut, dielectron studies can still be done as the contamination is less then 10%, and the PID efficiency is approximately 75% for $p < 2GeV/c$.

The results of the rectangular electron PID cut on MC data are shown in figure 2.12, 2.13, 2.14 and 2.15. In figure 2.12 the effects of the TPC pion rejection can be seen, before(left) and after(right) the rectangular PID cut. The black line is the imperical parametrization for pion rejection. By the $n\sigma_{\text{TPC}}^{e}$
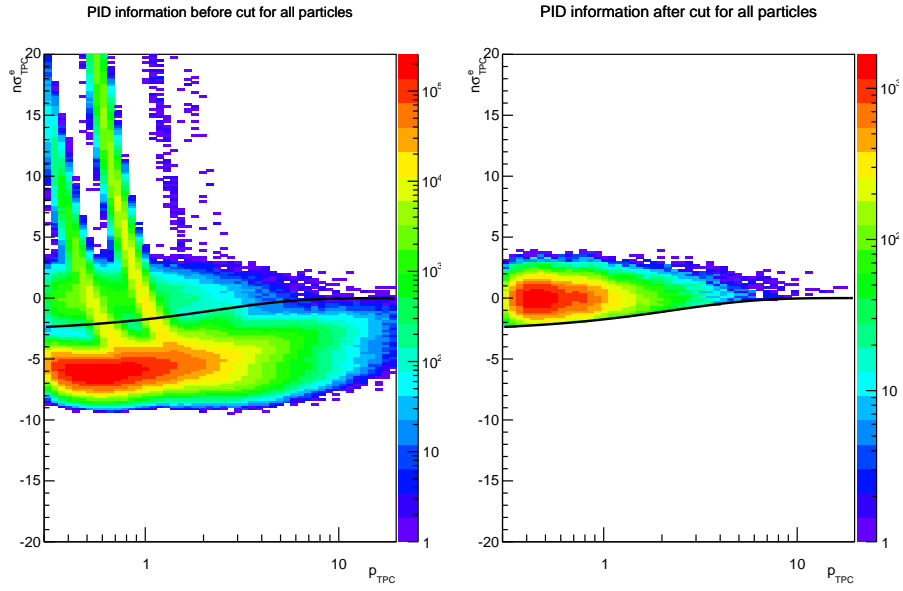
Figure 2.7: The distribution of $n\sigma^e_{\mathrm{TPC}}$ vs p for the MC simulation before and after the spherical electron PID cut
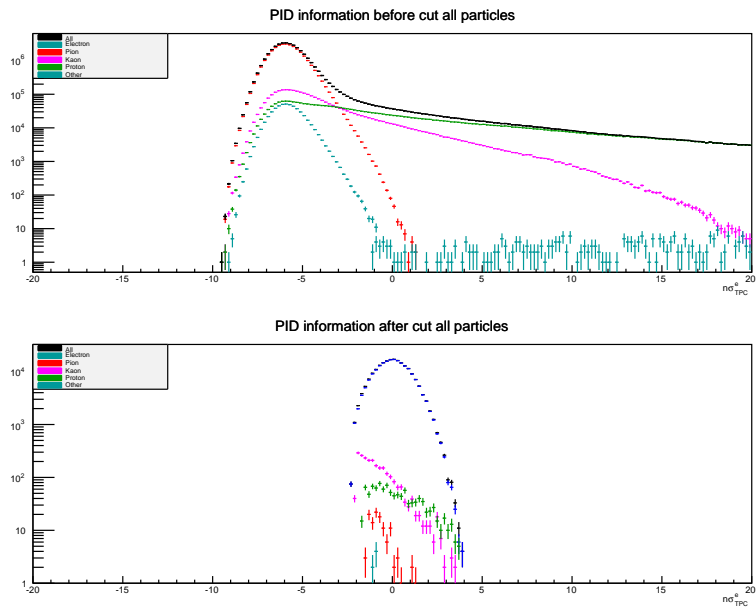

Figure 2.8: The distribution of of $n\sigma^e_{\mathrm{TPC}}$ for the MC simulation before and after the spherical electron PID cut.
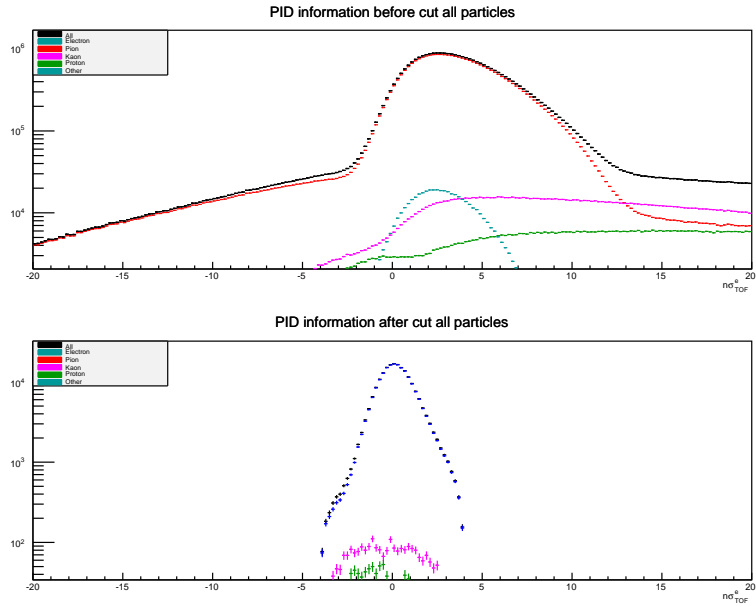
13

Figure 2.9: The distribution of $n\sigma^e_{\mathrm{TOF}}$ for the MC simulation before and after the spherical electron PID cut.
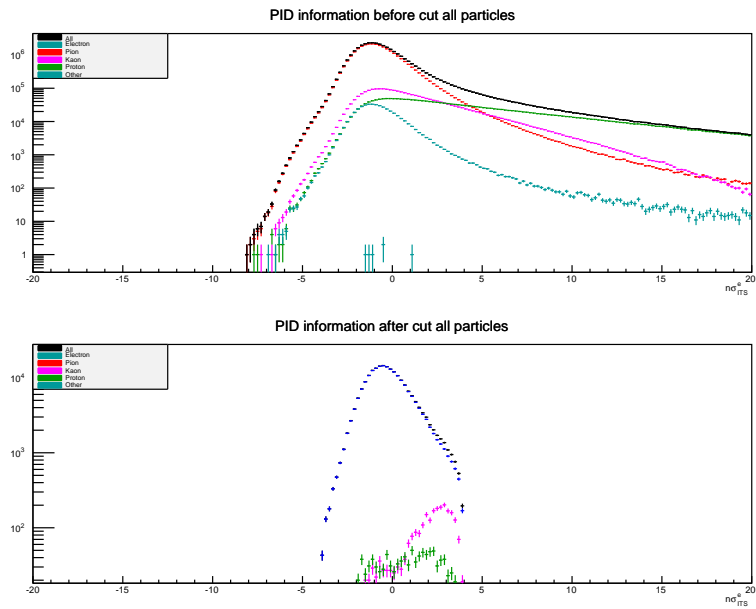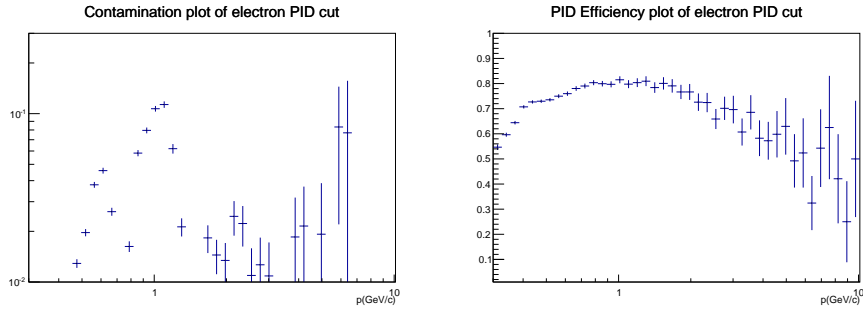

Figure 2.10: The distribution of $n\sigma^e_{\mathrm{ITS}}$ for the MC simulation before and after the spherical electron PID cut.

(a) The contamination of the rectangular electron PID cut.

(b) The PID efficiency of the rectangular electron PID cut.

Figure 2.11: The PID efficiency and contamination of the rectangular electron PID cut on MC simulations.

electron inclusion cut protons and kaons are also heavily rejected outside of a few momentum bin, which is also illustrated in figure 2.13, where the distribution of $n\sigma^e_{\mathrm{TPC}}$ can be seen for different particles.

Figure 2.14 further illustrates the reason for use of TOF, as the particles other then the electron have a more widespread distrbution before the rectangular PID cut(upper), and it can be seen in the lower figure that after the rectangular PID cut, they are significantly reduced. Figure 2.15 shows the neccesity of the ITS cut, as after the rectangular PID cut, there is a peak of the proton and the kaon distributions to the right of the $n\sigma^e_{\mathrm{ITS}}$ limit of the rectangular PID cut.

The effects on the PID distributions of the PID electron cut on real data are shown in figures 2.16, 2.17,2.18 and 2.19. Figures 2.16, 2.17 and 2.18 indicate in the lower or right figure that after the PID cut the $n\sigma^e_{TPC}$ and $n\sigma^e_{TOF}$ distributions have a peak around approximately 0, different from the shapes before the PID cut. The ITS distribution is still peaked at approximately $n\sigma^e_{\mathrm{ITS}} = 0$ after the PID cut, which can be seen in figure 2.19. So the shapes of the distributions indicate that the PID cut seperates electrons from other particles.

In a few p slices, the contamination (caused by particles which TPC can seperate from electrons) is calculated. This value was never higher then .01%, but does not take into account the bins in which convergence is nontrivial, and particles which the TPC does not seperate(for instance, protons at $p = 1GeV/c$). Two of these fits are shown in figure 2.20. This small contamination estimation also indicates that the PID cut seperates electrons from other particles.
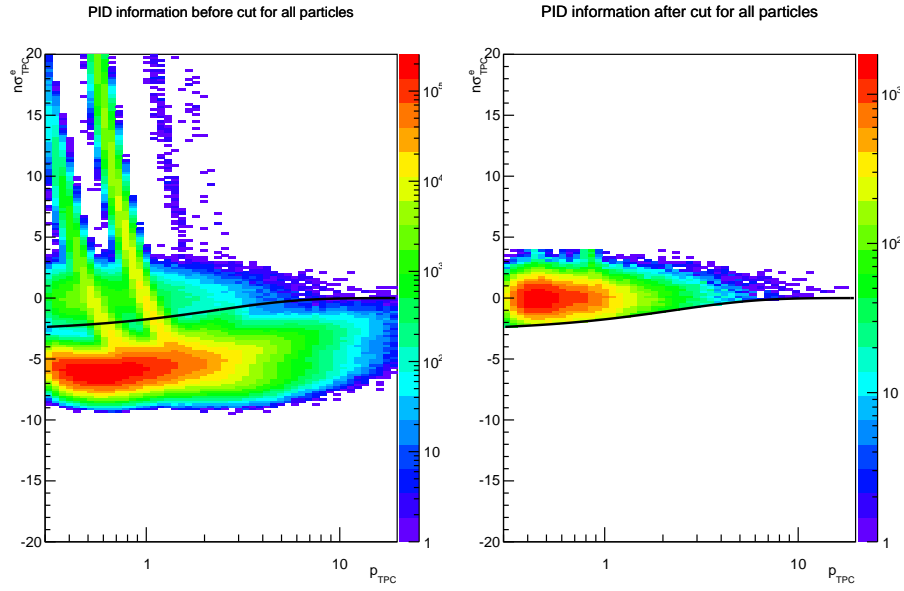
15

Figure 2.12: The distribution of $n\sigma^e_{\mathrm{TPC}}$ vs p for the MC simulation before and after the rectangular electron PID cut

Figure 2.13: The distribution of $n\sigma^e_{\mathrm{TPC}}$ for the MC simulation before and after the rectangular electron PID cut.
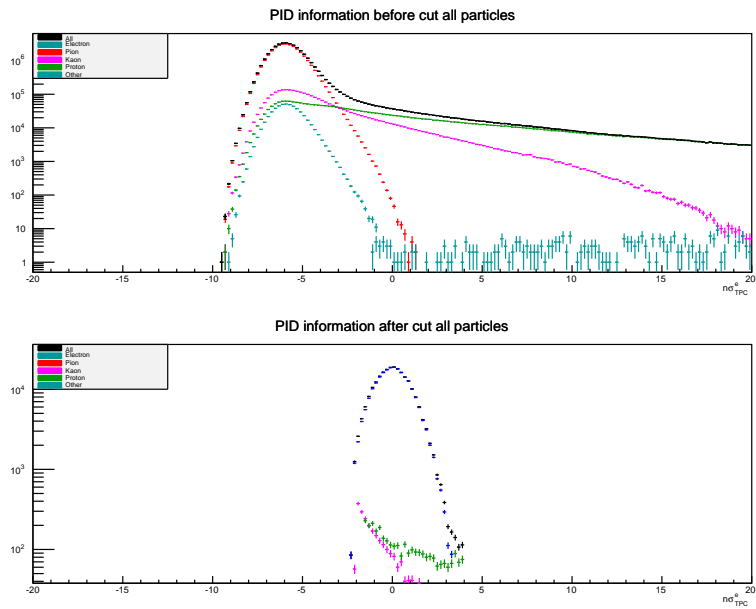
Figure 2.14: The distribution of $n\sigma^e_{\text{TOF}}$ for the MC simulation before and after the rectangular electron PID cut.
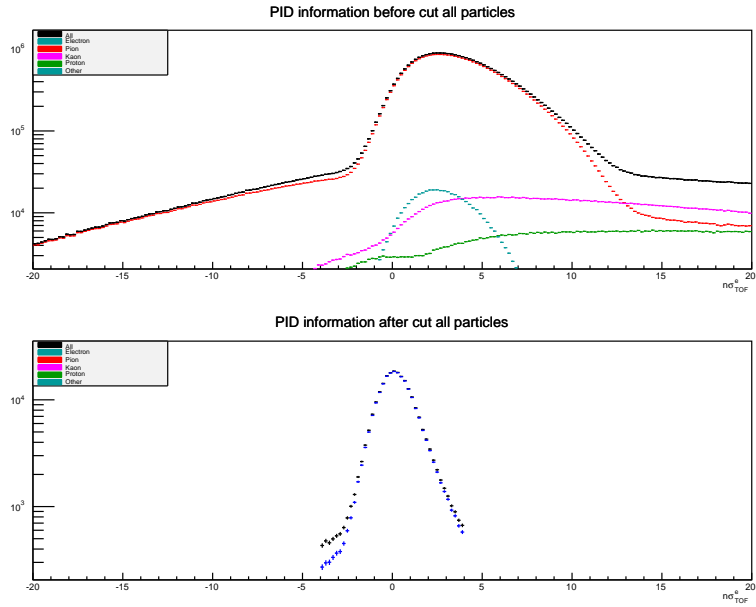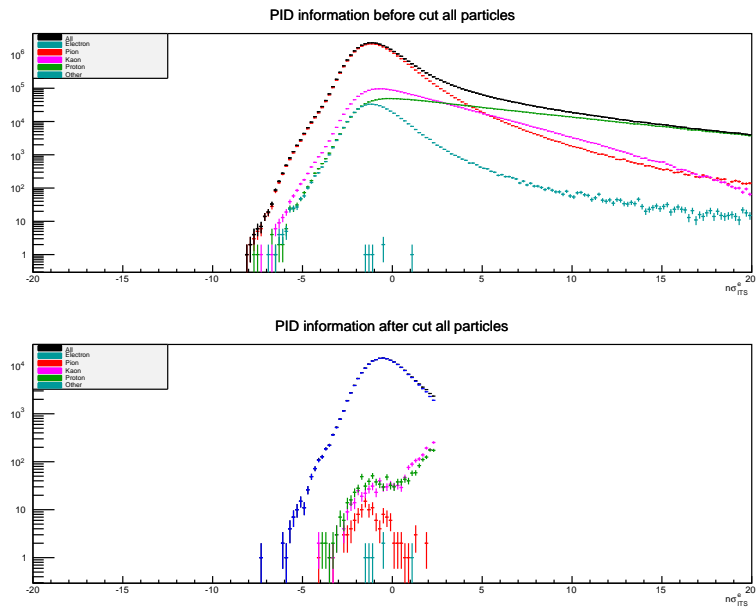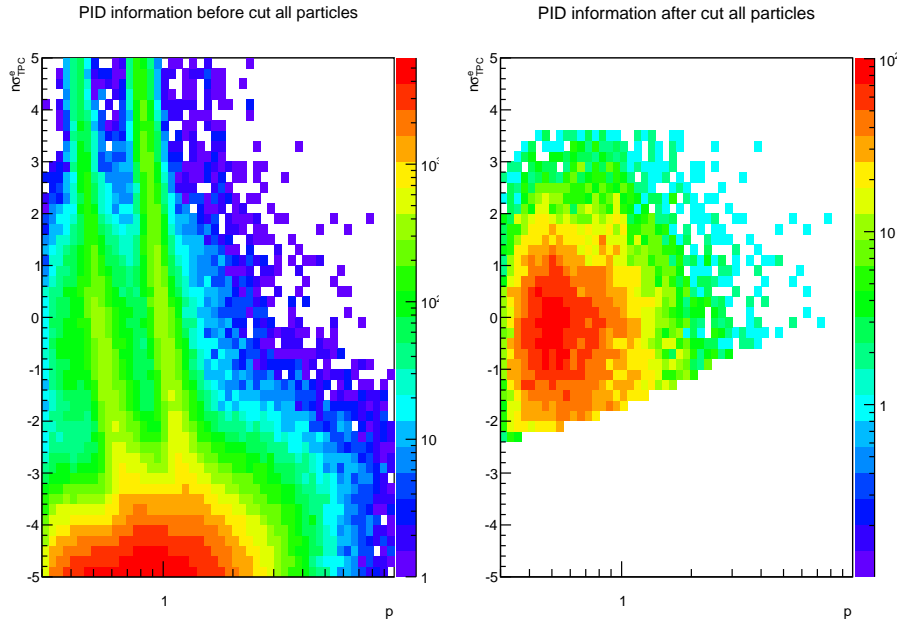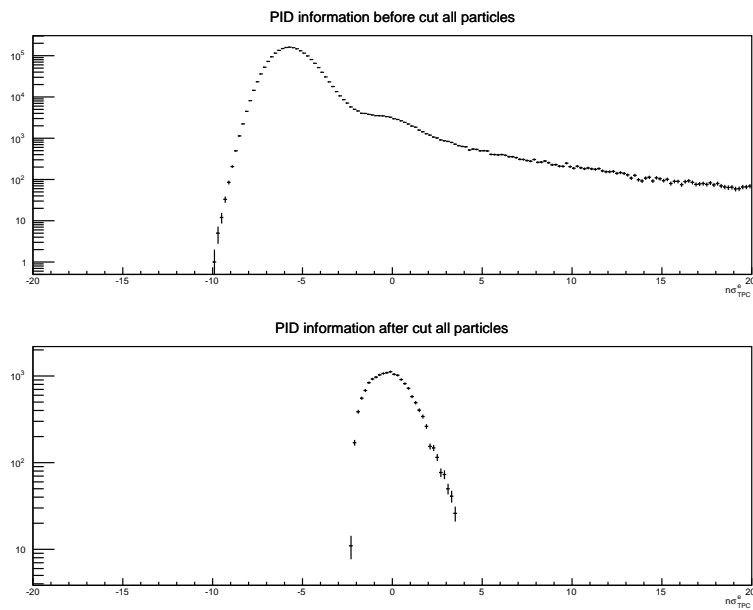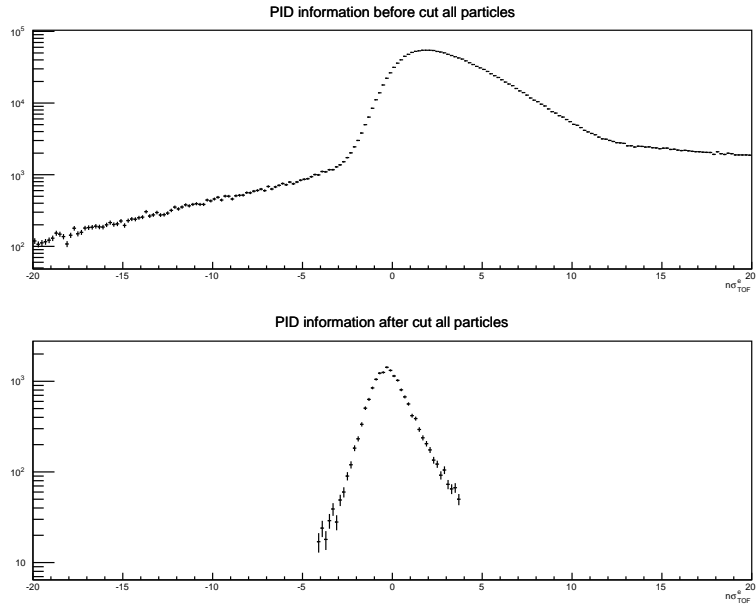

Figure 2.15: The distribution of $n\sigma^e_{\text{ITS}}$ for the MC simulation before and after the rectangular electron PID cut.

Figure 2.16: The distribution of $n\sigma^e_{\mathrm{TPC}}$ vs p for real data before and after the rectangular electron PID cut.

Figure 2.17: The distribution of $n\sigma^e_{\mathrm{TPC}}$(p integrated) for real data before and after the rectangular electron PID cut.

Figure 2.18: The distribution of $n\sigma^e_{\text{TOF}}$(p integrated) for real data before and after the rectangular electron PID cut.
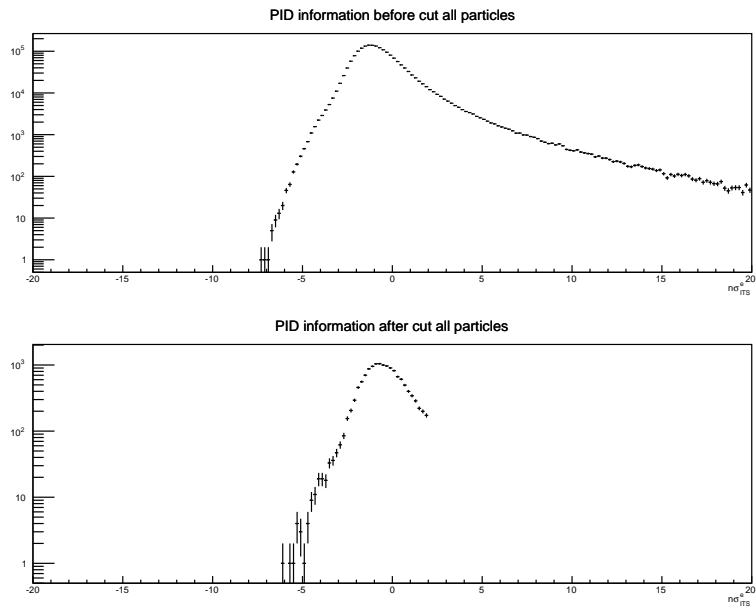

Figure 2.19: The distribution of $n\sigma^e_{\text{ITS}}$(p integrated) for real data before and after the rectangular electron PID cut.
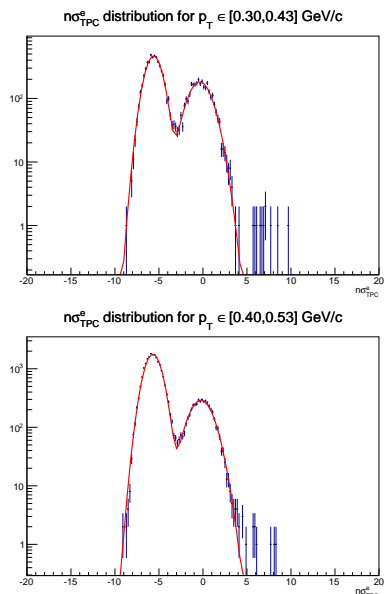
Figure 2.20: The distribution of $n\sigma^e_{\mathrm{TPC}}$ in certain p slices, for real data after the rectangular electron PID cut, without the TPC cuts. A double Gaussian fit of this histogram is done. This Gaussian fit is used to approximate contamination by particles which TPC can seperate from electrons. This contamination is never higher then 0.01%

2.4 Unfolding

With the identified electrons we can measure thier spectrum in the (p_T, η, ϕ) phasespace. However, this measured spectrum is not identical to the true spectrum, which contains the physics we are after. A naive way of obtaining the true spectrum is to use an efficiency correction, which can be calculated with MC simulations:

$$\epsilon_{\mathrm{bin}\ i} = \frac{N_{\mathrm{reconstructed\ in\ bin}\ i}}{N_{\mathrm{generated\ in\ bin}\ i}}$$

This operation is naive because it fully ignores all correlations between bins in phasespace. Tracks which belong in a certain true bin in the (p_T, η, ϕ) phasespace, get distributed over a number of bins in the measured spectrum. The distribution for every bin is the so called detector response (which we denote by $R(m, t)$, the probability of a track in true bin t to end up in measured bin m). So rather than just multiplying every bin with an efficieny correction, a different method needs to be used. Methods that can help us to achieve this are called unfolding methods.

2.4.1 Theory

A priori the measured distribution $M(m)$ and the detector response $R(m, t)$ are known. The detector response can be extracted from simulations, or obtained by calibration of the detector. A detector response generated from the same

dataset that I will use is illustrated in figure 2.21. From the measured spectrum and the detector response, we wish to extract the true spectrum $T(t)$. For high enough statistics, we can expect:

$$M(m) = \sum_t R(m,t)T(t)$$

by definition of $R(m,t)$.

One might guess that inversion of the matrix $R(m,t)$ should be enough to get $T(t)$ from $M(m)$, but this is often not true. The matrix $R(m,t)$ might not be invertible, but even if it is, it might result in a true spectrum $T(t)$ that looks nothing like the spectrum you might expect. Because of the resolution effect, high variance may occur in the data, as this can be compensated for in neighbouring bins[8].

Unfolding algorithms can unfold the reconstructed spectrum of tracks into the true spectrum of measured tracks, after which an effective efficiency correction. This effective efficiency correction is defined as:

$$\epsilon_{\text{bin } i} = \frac{N_{\text{reconstructed in bin } i}}{N_{\text{generated in bin } i}}$$

This effecitve efficiency correction is also obtained from MC simulations. By dividing the unfolded spectrum by this effective efficiency correction, the true spectrum can be obtained. The unfolding algorithms can take into account the efficiency correction by scaling the detector response(by the efficiency correction), but in this thesis this is not considered to reduce computational complexity.

Bayesian Unfolding

One of the algorithms to unfold is called Bayesian Unfolding(known in other fields as Richardson-Lucy deconvolution[9]), proposed in use for particle physics by d'Agostini[10]. This method is named after Bayes law:

$$P(T|M) = \frac{P(M|T)P(T)}{P(M)}$$

In our notation, this is(normalization to make the spectrum a chance is not necessary, as the true spectrum has the same amount of particles as the measured spectrum):

$$\tilde{R}(m,t) = \frac{R(m,t)T(t)}{M(m)}$$

with $\tilde{R}(m,t)$ being the matrix that corresponds with the true "response" given a certain measured value. Because $M(m) = \sum_{t'} R(m,t')T(t')$ this can be written as:

$$\tilde{R}(m,t) = \frac{R(m,t)T(t)}{\sum_{t'} R(m,t')T(t')}$$

Then because $T(t) = \sum_m \tilde{R}(m,t)M(m)$ we know that:

$$T(t) = \sum_m \frac{R(m,t)T(t)M(m)}{\sum_{t'} R(m,t')T(t')}$$

This relation on its own is not useful. However, iteration over this algorithm is possible:

$$T_{n+1}(t) = \sum_m \frac{R(m,t)T_n(t)M(m)}{\sum_{t'} R(m,t')T_n(t')}$$

It has been shown (by applying this strategy on simulations[9][10]) that when iterating with this algorithm there is not only convergence, but convergence to the true distribution.

Minimization with regularization

Another method of unfolding is considering the χ^2 of the true spectrum $T_i(t)$, which is defined as:

$$\chi^2 = \sum_m \left(\frac{M(m) - \sum_t R(m,t)T(t)}{e(m)} \right)^2$$

with $e(m)$ as the error in the measurement. Note that this is the same χ^2 as the χ^2 for goodness of fit. This can be explained by considering that the χ^2 minimization as a fit. The bins of true spectrum are the parameters of the fitfunction, and the fitted function is $\sum_t R(m,t)T(t)$.

Minimization of this factor will only result in something similar to calculating the inverse, however. To emphasize the smoothness of the spectrum to the minimizer, an extra term called a regularization term is required.

Many regularization terms can be used. The choice of regularization mostly depends on what kind of smoothness you expect from your spectrum. A few possible regularization terms are

$$\sum_i \sum_t \left(\frac{(U(t) - U(t+e_i))}{U(t)} \right)^2 \tag{2.1}$$

$$\sum_i \sum_t \left(\frac{2U(t) - U(t+e_i) - U(t-e_i)}{U(t)} \right)^2 \tag{2.2}$$

$$\sum_i \sum_t \left(\frac{2\ln(U(t)) - \ln(U(t+e_i)) - \ln(U(t-e_i))}{\ln(U(t)} \right)^2 \tag{2.3}$$

where e_i is the unit vector in direction i. These regularization terms are added to the χ^2 term after being multiplied by a constant, the regularization factor.

2.4.2 Method

Unfolding was applied on the 3-dimensional (p_T, η, ϕ) spectrum of electrons identified with the PID method discussed eariler. To compensate for possible correlations, the whole spectrum was unfolded, rather than just the projections(if the (p_T, η, ϕ) distributions of electrons are truly independent, then this is not necessary). The 3-dimensional spectrum contains more information as well, since for instance for electrons in every η bin we know their p_T distribution.
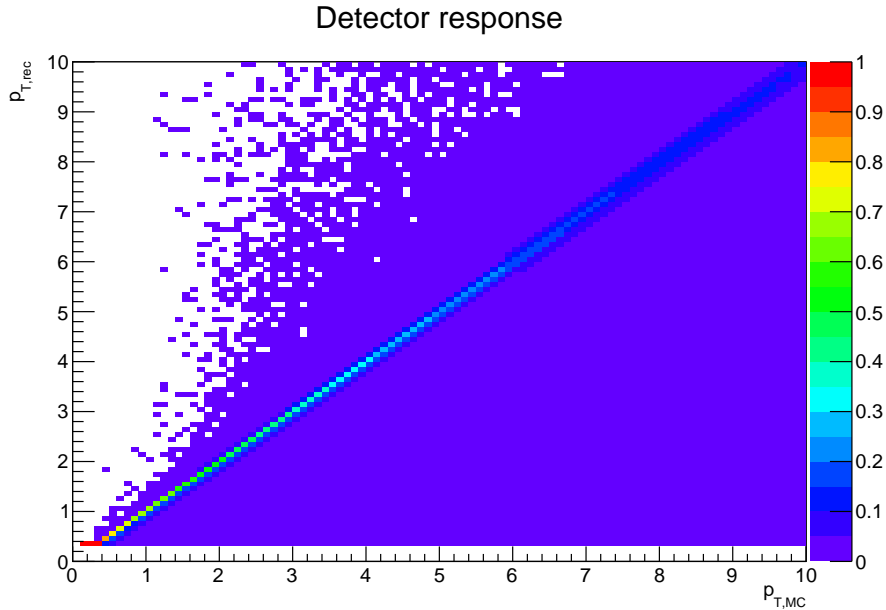
Figure 2.21: The detector response for p_T for PID electrons can be seen here. Note that this is not a projection of a 3-dimensional detector response, as such a projection would not be normalized.

The detector response was extracted from the simulations for the same collision system and centrality bin (explained in 2.2). Because the data is 3-dimensional, the detector response is 6-dimensional. The effective efficiency was also extracted using this simulation. The effective efficiency is used to correct data from the unfolded spectrum.

For Bayesian unfolding, the convergence criterion used for this thesis is that $\sum_t \left(\frac{T_n(t) - T_{n-1}(t)}{T_{n-1}(t)} \right)^2 < 0.00001 \cdot N$ with N the number of bins(as described in [8]). The error is calculated by slightly changing the measurement(using a Poisson distribution for every bin) and then unfolding again[8].

χ^2 unfolding with regularization has been simplified because of convergence issues. Only the p_T dimension was unfolded. Regularization term 2.1 was used, with a regularization factor of 10^5.

For testing the unfolding on the simulated data, the dataset is splitted in two halves, with one part used for the detector response, and the other half for the data to be unfolded. The data is splitted because otherwise the detector response would be perfect for the given dataset, and that means that the simulated result is not representative for the real result.

2.4.3   Results

Testing Bayesian unfolding with simulated data

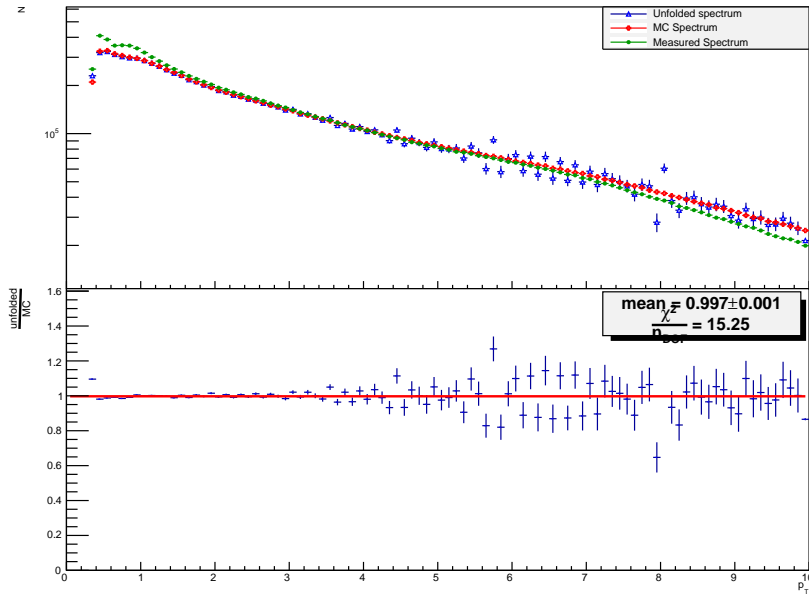A 2-dimensional detector response generated from the same data is shown in figure 2.21.

Figure 2.22: The results for 3-dimensional Bayesian unfolding on MC PID e^- and a comparison with the MC spectrum of reconstructed tracks, projected to the p_T axis.
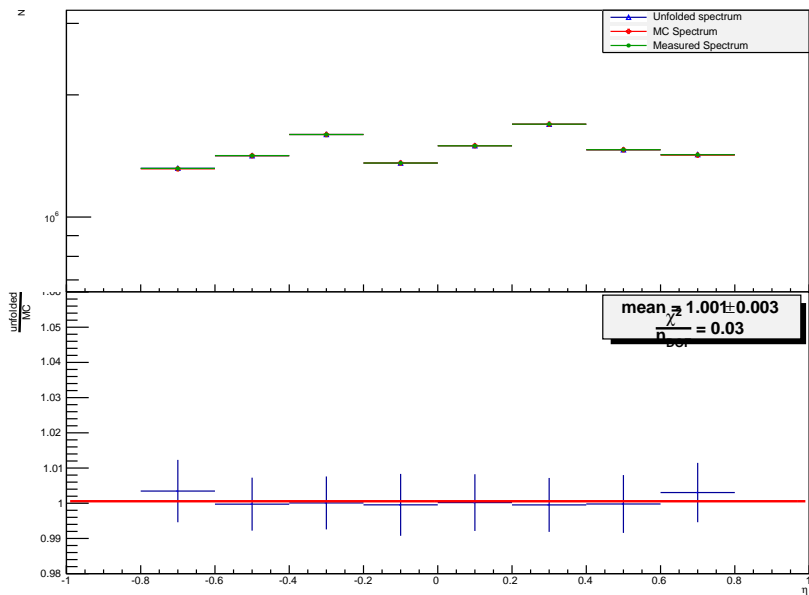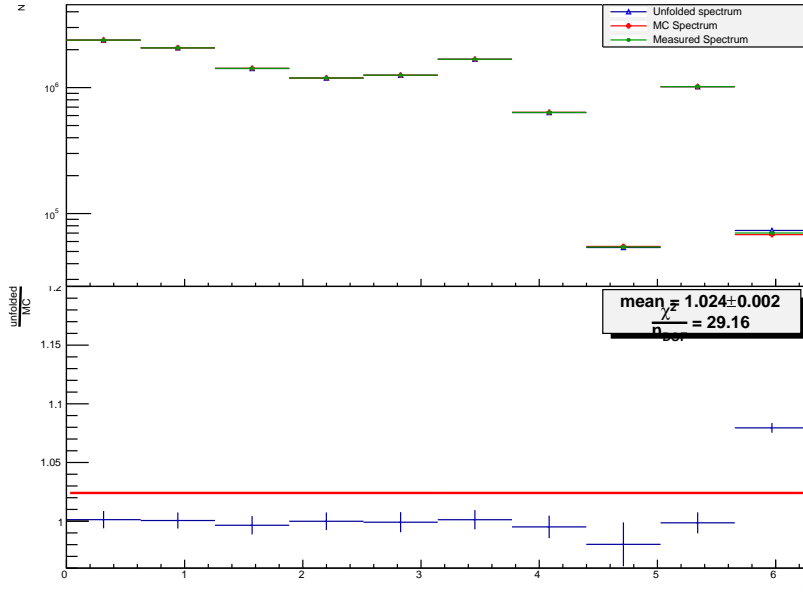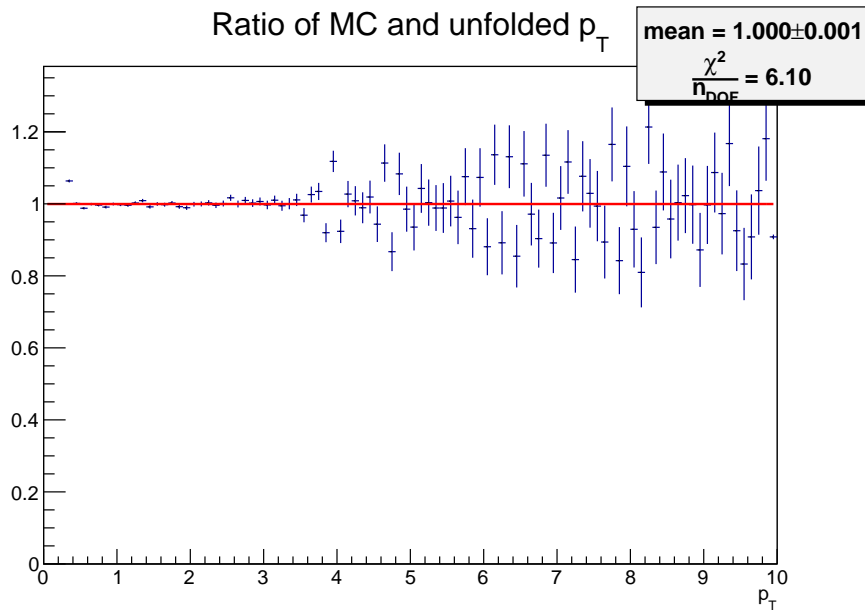

Figure 2.23: The results for 3-dimensional Bayesian unfolding on MC PID e^- and a comparison with the MC spectrum of reconstructed tracks, projected to the η axis.

Figure 2.24: The results for 3-dimensional Bayesian unfolding on MC PID e^- and a comparison with the MC spectrum of reconstructed tracks, projected to the ϕ axis.

Figure 2.25: The comparison of the result of 3-dimensional Bayesian unfolding on MC PID e^+ with the MC spectrum of tracks of the p_T direction.
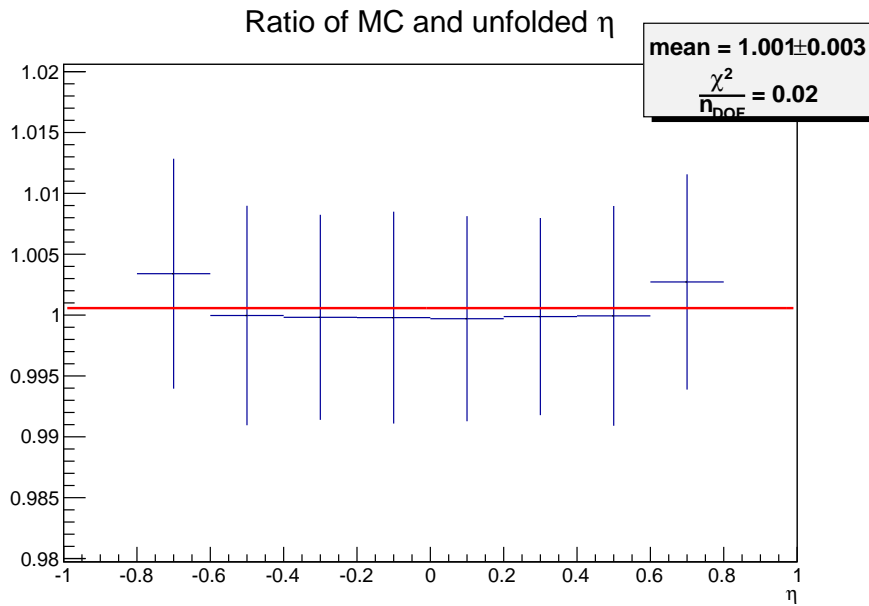
Figure 2.26: The comparison of the result of 3-dimensional Bayesian unfolding on MC PID e^+ with the MC spectrum of tracks of the η direction.
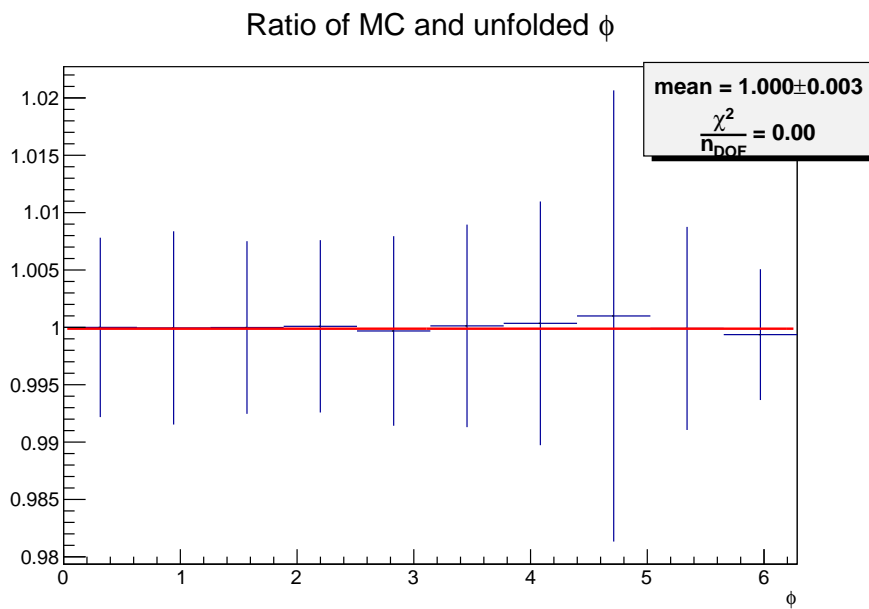

Figure 2.27: The comparison of the result of 3-dimensional Bayesian unfolding on MC PID e^+ with the MC spectrum of tracks of the ϕ direction.
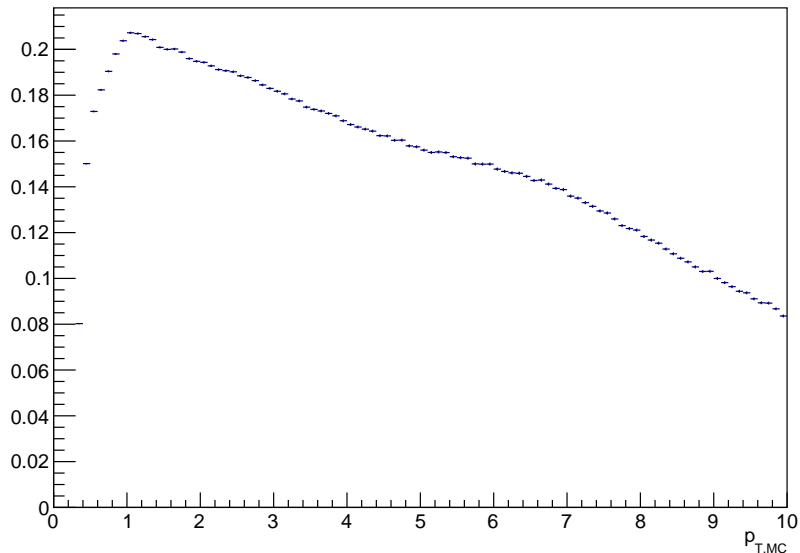
Figure 2.28: The efficieny of the p_T spectrum.

The results of the Bayesian unfolding of MC data using a 6-dimensional response can be seen in figures 2.22, 2.23 and 2.24 for e^-, and in figure 2.25, 2.26 and 2.27 for e^+. The unfolded spectra for η and ϕ(in figures 2.23 and 2.24 for e^-, and 2.23 and 2.24 for e^+, respectively) are very consistent with MC, besides one ϕ bin for e^-, as they are all nearly 1. The error for the ϕ bin could possibly be explained by the errors of the detector response.

For the p_T spectrum, visible in figure 2.22 and 2.25, the ratio of MC and unfolded as also approximately 1. However, there are big oscillations in the p_T spectrum above 3 GeV/c, for both e^- and e^+. These oscillations might also be caused by errors in the detector response, or by the algorithm. Because neighbouring bins are heavily correlated, spectra with oscillations can produce the same spectrum as those without[8].

This unfolded result has been corrected for efficiency. The efficiency correction is illustrated in figures 2.28, 2.29 and 2.30, where the efficiency corrections of projections are drawn(not the projections of the efficiency, as those would not be normalized, but the efficiency corrections used when unfolding only one dimension). Note that these figures do not display correlations, but these correlations have been taken into account. The efficiency corrected spectra can be seen in figures 2.31, 2.32 and 2.33. Similar effects are visible as in the spectra without efficiency correction, as these are merely a multiplication of these spectra.

Testing unfolding with regularization with simulated data

Unfolding with χ^2 minimization has been looked at in less detail than the Bayesian unfolding. The results of one-dimensional χ^2 unfolding with linear regularization(regularization term 2.1), with a regularization factor of 10^5, are
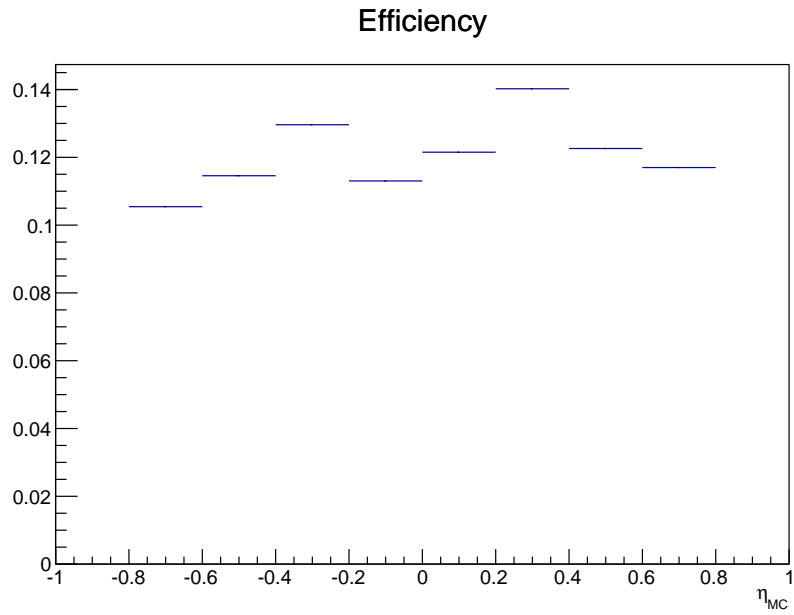
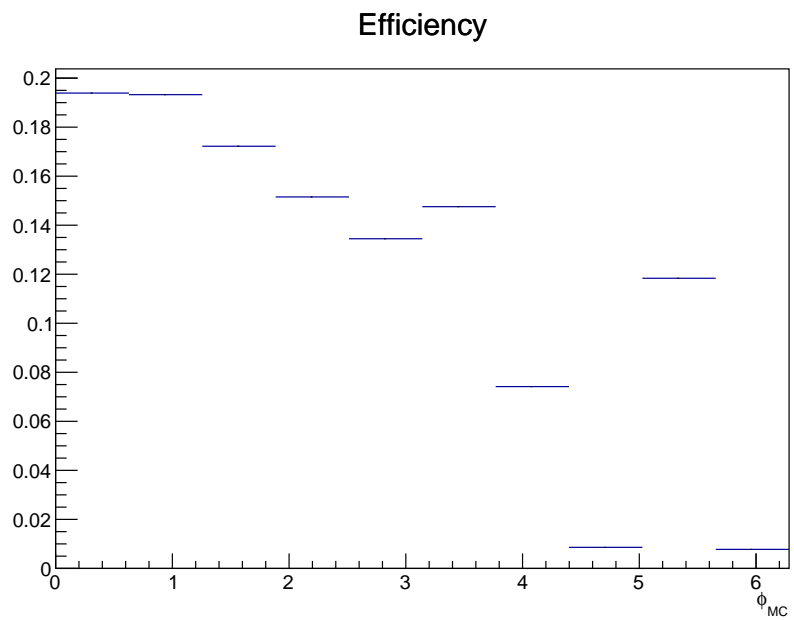Figure 2.29: The efficieny of the η spectrum.

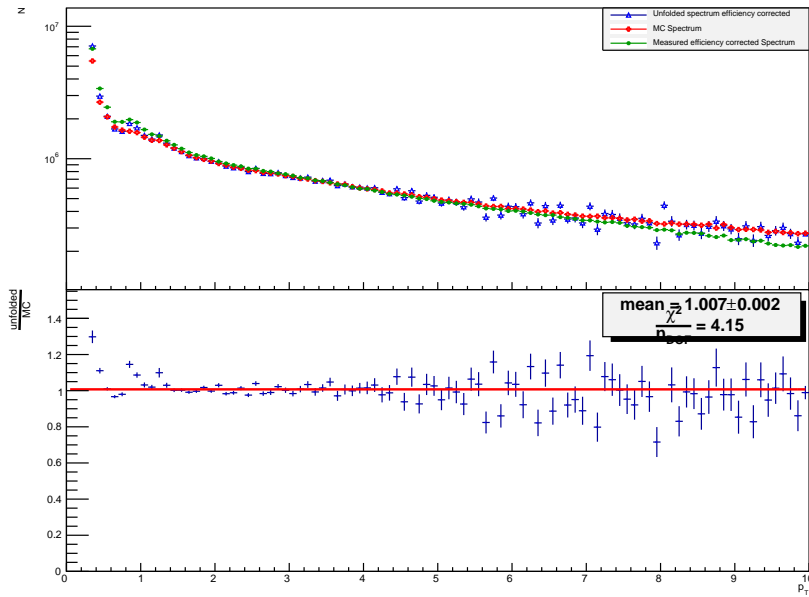Figure 2.30: The efficieny of the ϕ spectrum.

Figure 2.31: The results for 3-dimensional Bayesian unfolding on MC PID e^- after an efficiency corretion and a comparison with the MC spectrum of particles, projected to the p_T axis. As a comparison, the measured spectrum has also been given the same efficiency correction(which is the naive way to do this).
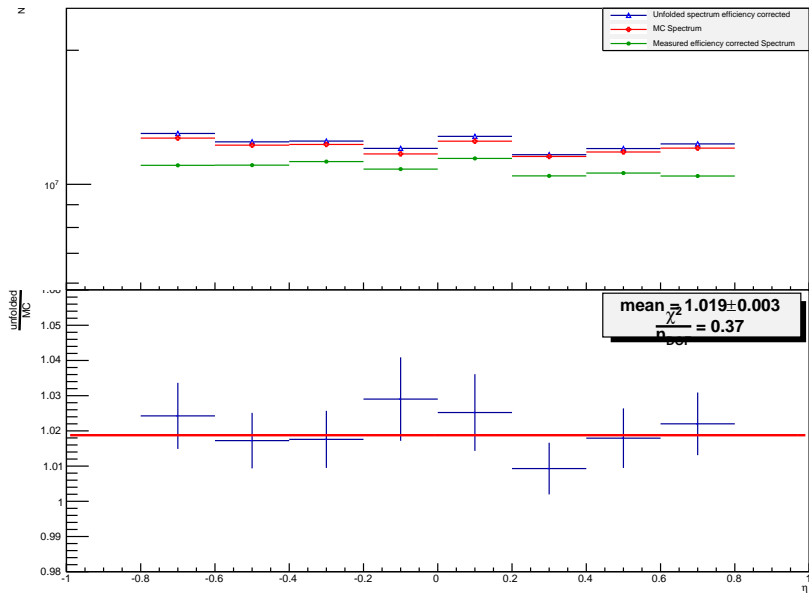

Figure 2.32: The results for 3-dimensional Bayesian unfolding on MC PID e^- after an efficiency corretion and a comparison with the MC spectrum of particles, projected to the η axis. As a comparison, the measured spectrum has also been given the same efficiency correction(which is the naive way to do this)
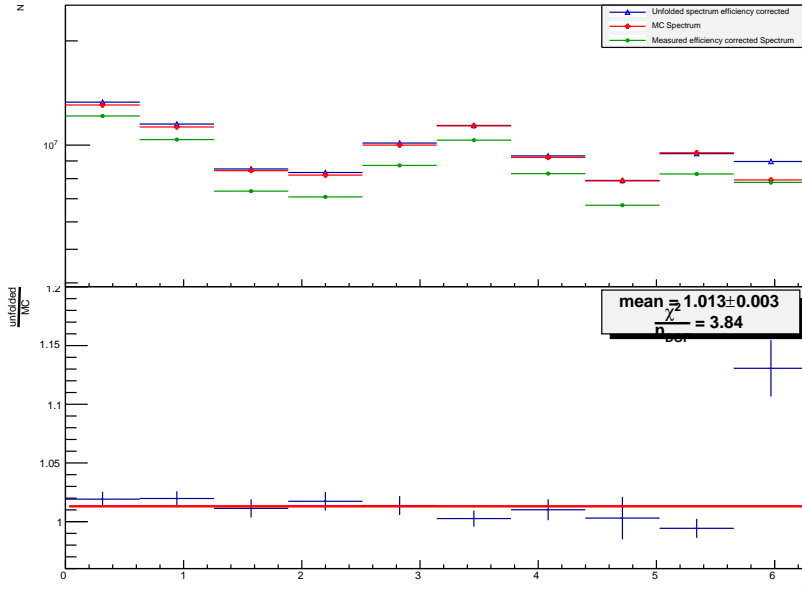
Figure 2.33: The results for 3-dimensional Bayesian unfolding on MC PID e^- after an efficiency corretion and a comparison with the MC spectrum of particles, projected to the ϕ axis. As a comparison, the measured spectrum has also been given the same efficiency correction(which is the naive way to do this).

shown in figure 2.34. For the moment, technical issues with the minimizer prevent the calculation of errors. This can be investigated given extra time. Figure 2.34 shows that the one-dimensional χ^2 unfolding with regularization provides a lot less oscillations then the Bayesian unfolding(figure 2.22). This may be caused by the dimensionality of the problem, but it seems more reasonable that the regularization term reduces these oscillations.

Unfolding of real data

The results of the Bayesian unfolding can be seen in figures 2.35,2.36,2.37,2.38,2.39 and 2.40. The unfolding does not seem to have much effect in all these figures. This could be caused by the use of a detector response that does not correspond to the real detector response. Because MC is used in this thesis for the detecor response, imperfections in simulations can be the cause of this effect.
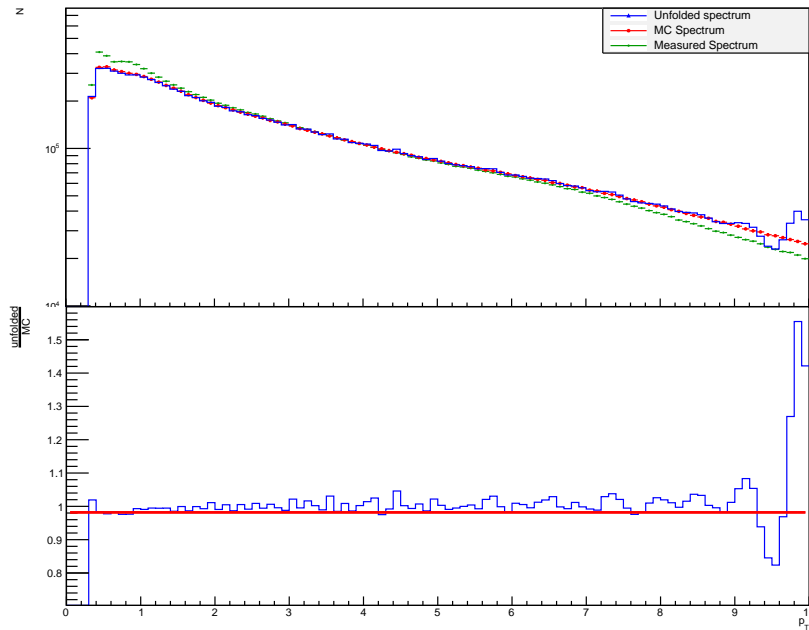
Figure 2.34: The result of 1-dimensional χ^2 unfolding with lineair regularization, with regularization factor of 10^5, compared to the MC tracks and the measured spectrum. A comparison with the MC spectrum is also added(with the mean/a fit of a constant drawn). The errors are not calculated because of a technical issue with the minimizer.
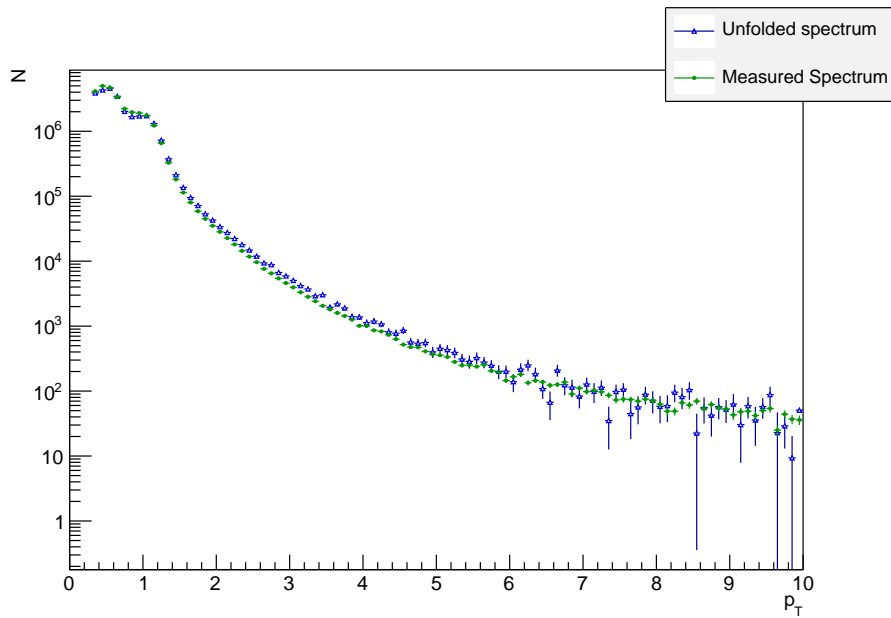

Figure 2.35: The results for 3-dimensional Bayesian unfolding on real data without efficiency correction, projected to p_T.
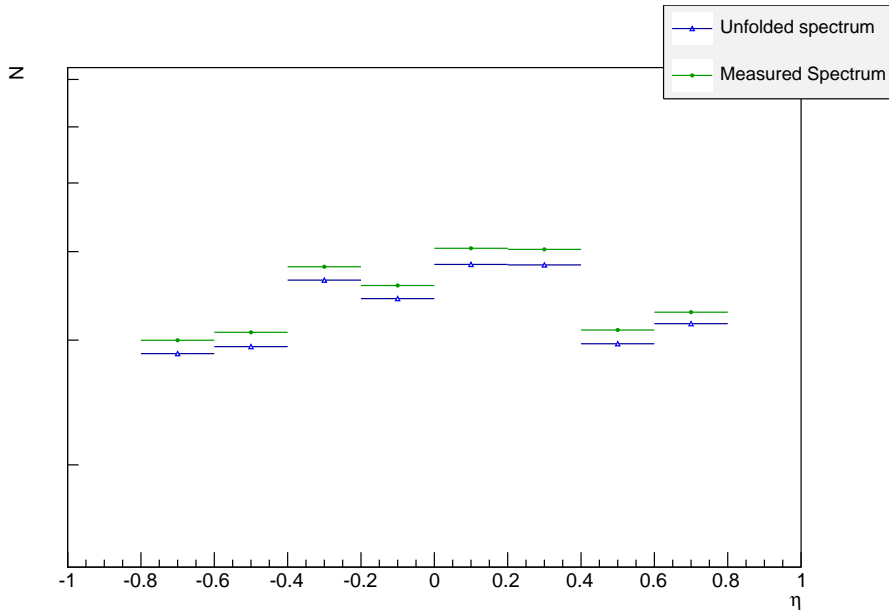
Figure 2.36: The results for 3-dimensional Bayesian unfolding on real data without efficiency correction, projected to η.
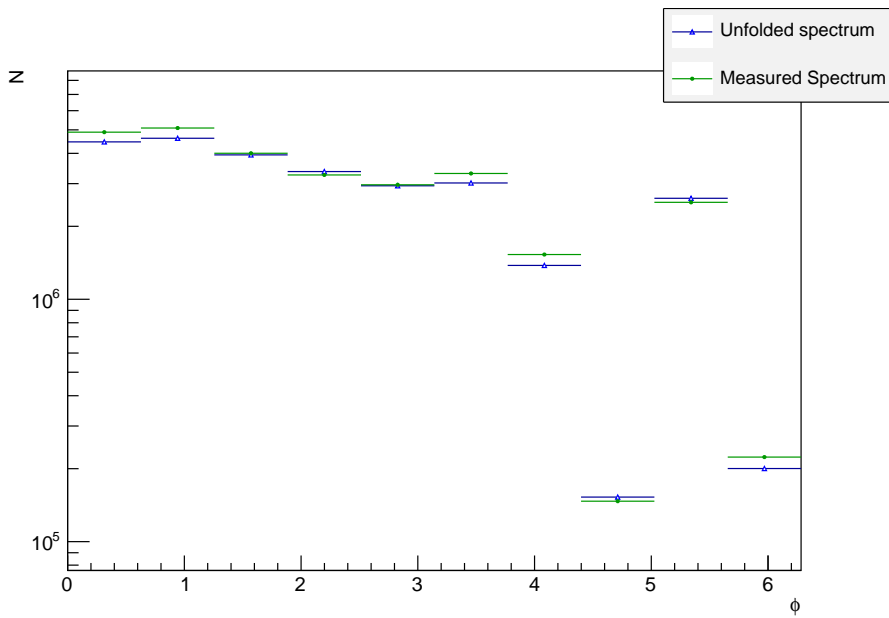

Figure 2.37: The results for 3-dimensional Bayesian unfolding on real data without efficiency correction, projected to ϕ.

Figure 2.38: The results for 3-dimensional Bayesian unfolding on real data with efficiency correction, projected to p_T. As a comparison, the measured spectrum has also been given the same efficiency correction(which is the naive way to do this).
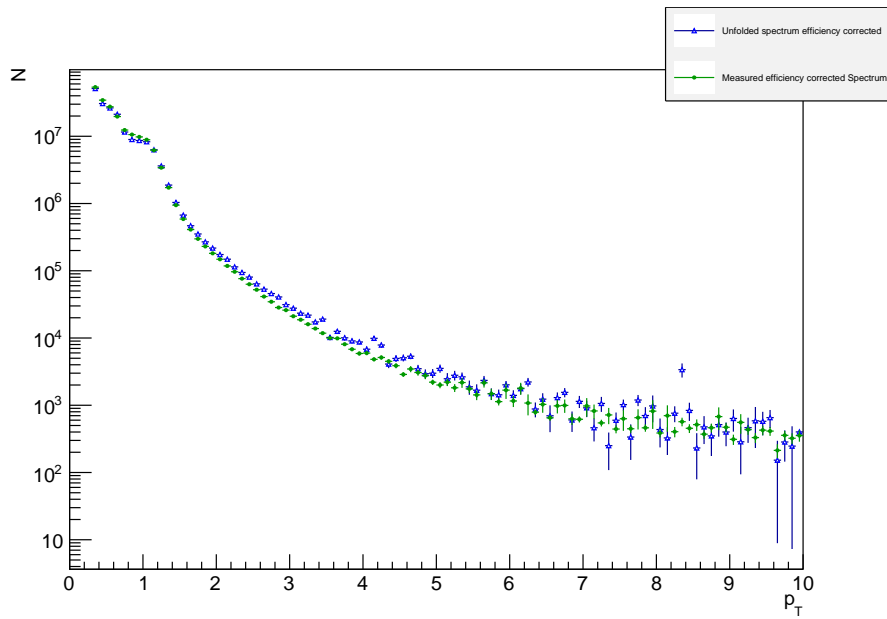

Figure 2.39: The results for 3-dimensional Bayesian unfolding on real data with efficiency correction, projected to η. As a comparison, the measured spectrum has also been given the same efficiency correction(which is the naive way to do this).

Figure 2.40: The results for 3-dimensional Bayesian unfolding on real data with efficiency correction, projected to ϕ.As a comparison, the measured spectrum has also been given the same efficiency correction(which is the naive way to do this).
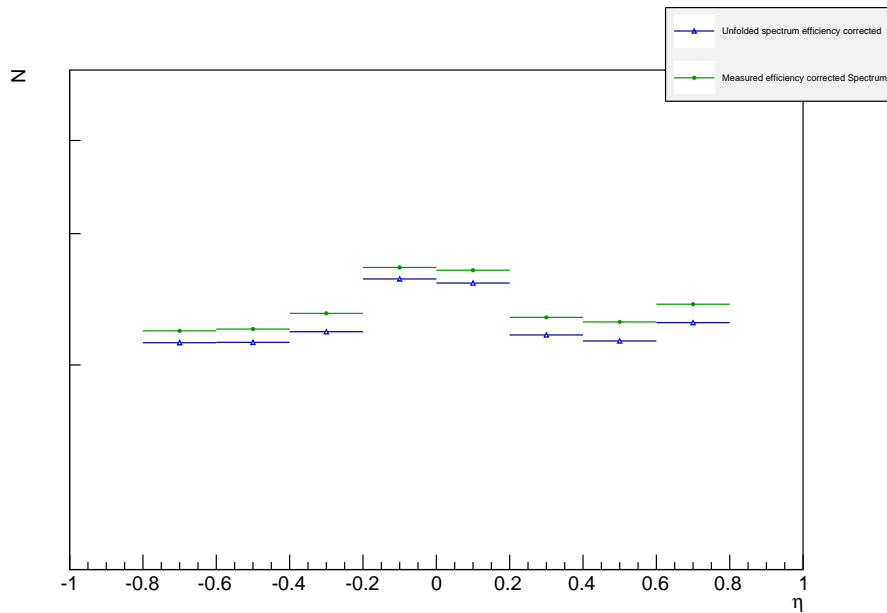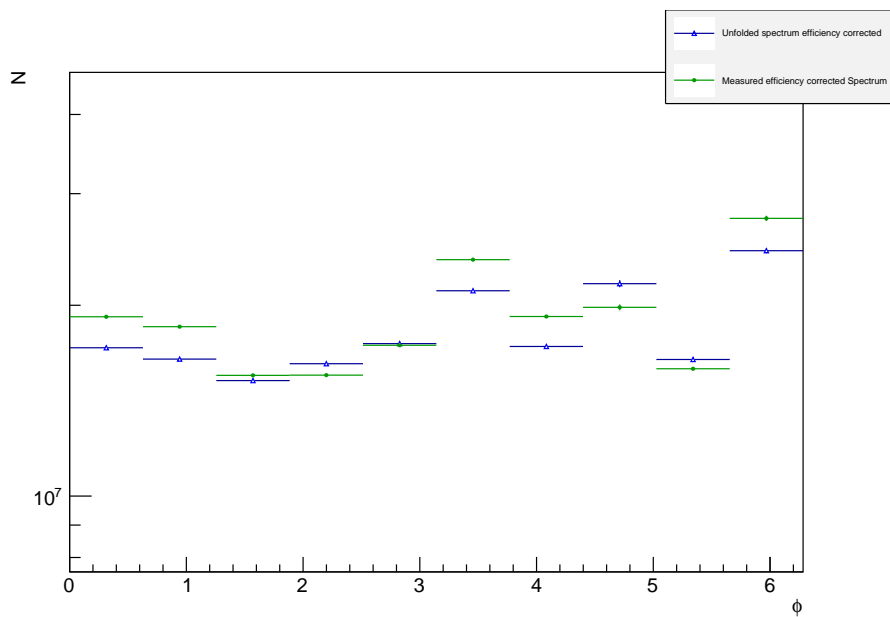
Chapter 3

Conclusion and Summary

3.1 Conclusion and Outlook

The Bayesian unfolding still works to some degree with the amount of bins used in this thesis, as the results are clearly better than just an efficiency correction. However, the result has a lot of variance. This may be fixed by smoothing the eventual histogram, by averaging over nearby bins(for instance $T(t) = (1 - \alpha)T(t) + \frac{\alpha}{3n} \sum_{i=1}^{n} T(t + e_i) + T(t) + T(t - e_i)$ with α a smoothing factor, e_i the unit vector in the ith direction, and n the number of dimensions). This should fix many of the issues present in the current Bayesian method, as shown in figure 2.22.

The χ^2 minimization unfolded spectrum on the other hand looks great, but this spectrum is not unfolded 3-dimensionally. The χ^2 minimization can be extended to a multidimensional case, see section 2.4.1.

The effect of the detector resonse is not studied in this thesis, whcih can be added by iterating over multiple variations of the detector response, given more time.

It seems that the Bayesian algorithm is not really useful for unfolding datasets with large amount of bins, as the part of the algorithm that used to prevent large fluctuations, seems to be limited for higher statistics. The χ^2 minimization algorithm looks like a promising solution to solve this.

3.2 Summary

To investigate such the hot and dense matter states created in heavy ion collisions, we can use electron pairs produced from conversions of virtual photon with the ALICE experiment. For this purpose, electron identification methods are studied with both MC and real data. Electrons can be selected by making use of the detectors ITS, TPC and TOF in ALICE. We can use multiple algorithms to compensate for the detector resolution in the measurements, such algorithms are called unfolding algorithms. Simply multiplying by an efficiency is not a good way to get the true spectrum. Bayesian and χ^2 minimization algorithms are discussed and used in this thesis.

Bibliography

[1] Ernest M. Henly, Alejandro Garcia, *Subatomic Physics*, World Scientific Publishing, Singapore, 3rd edition, 2007

[2] The ALICE Collaboration, *TPC Techinical Design Report* December 1999

[3] ALICE TWiki, *PWGPPParticleIdentification*, `https://twiki.cern.ch/twiki/bin/view/ALICE/PWGPPParticleIdentification`,

[4] The ALICE Collaboration, *The ALICE Time of Flight Detector*, `http://aliceinfo.cern.ch/Public/en/Chapter2/Chap2_TOF.html`,

[5] The ALICE Collaboration, *The ALICE Silicon Pixel Detector*, `http://aliceinfo.cern.ch/Public/en/Chapter2/Chap2_SPD.html`,

[6] Marek Chojnacki, *Measurement of pions, kaons and protons with the ALICE detector in pp collisions at the LHC*

[7] ALICE TWiki, *CentStudies*, `https://twiki.cern.ch/twiki/bin/viewauth/ALICE/CentStudies`,

[8] J.F. Grosse-Oetringhaus, *Measuring the charged particle multiplicity distribution with the ALICE detector*, 9July 2008, ALICE-INT-2008-002

[9] W.H. Richardson, *Bayesian-Based Iterative Method of Image Restoration*, Journal of the Optical Society of America volume 62 number 1(January 1972) p55-59

[10] G.D' Agostini, *A multidimensional unfolding method based on Bayes' theorem*, Nuclear Instruments and Methods in Physics Research A 362 (1995) 487-498

[11] CERN, *Heavy ions and quark-gluon plasma*, `http://home.web.cern.ch/about/physics/heavy-ions-and-quark-gluon-plasma`

[12] CERN, *ALICE*, `http://home.web.cern.ch/about/experiments/alice`

[13] Scottish Universities' Summer School, *Heavy Ion Physics at the LHC*, 18-29 August 2003

[14] CERN, *The Large Hadron Collider* `http://home.web.cern.ch/topics/large-hadron-collider`

[15] Wikipedia, *Pseudorapidity* `http://en.wikipedia.org/wiki/Pseudorapidity`